LETTERS
PUBLISHED ONLINE: 21 OCTOBER 2012 | DOI: 10.1038/NMAT3462
nature materials

Atomic-scale determination of surface facets in gold nanorods

Bart Goris[1], Sara Bals[1]*, Wouter Van den Broek[1,3], Enrique Carbó-Argibay[2], Sergio Gómez-Graña[2], Luis M. Liz-Marzán[2] and Gustaaf Van Tendeloo[1]

It is widely accepted that the physical properties of nanostructures depend on the type of surface facets[1,2]. For Au nanorods, the surface facets have a major influence on crucial effects such as reactivity and ligand adsorption and there has been controversy regarding facet indexing[3,4]. Aberration-corrected electron microscopy is the ideal technique to study the atomic structure of nanomaterials[5,6]. However, these images correspond to two-dimensional (2D) projections of 3D nano-objects, leading to an incomplete characterization. Recently, much progress was achieved in the field of atomic-resolution electron tomography, but it is still far from being a routinely used technique. Here we propose a methodology to measure the 3D atomic structure of free-standing nanoparticles, which we apply to characterize the surface facets of Au nanorods. This methodology is applicable to a broad range of nanocrystals, leading to unique insights concerning the connection between the structure and properties of nanostructures.

A thorough understanding of the atomic structure of free-standing nanocrystals and the formation of facets at their surface is required to optimize their properties. For Au nanocrystals, it is known that the catalytic and optical properties can be tuned in a reproducible manner by controlling their morphology[7,8]. Surface morphologies of nanocrystals can be characterized in three dimensions using electron tomography[9–11], but often the resolution is insufficient to allow a straightforward characterization of the crystallographic planes at the surface. Significant progress, pushing the resolution in three dimensions to the atomic level, has recently been achieved[12–14]. On the basis of a limited number of high-angle annular dark-field scanning transmission electron microscopy (HAADF-STEM) images, a 3D reconstruction at the atomic scale could be obtained for a Ag nanoparticle with a diameter of approximately 3 nm, which was embedded in an Al matrix. These results were obtained using advanced statistical parameter estimation and so-called discrete tomography[12]. This approach was based on the assumption that all atom positions are fixed on a grid and this has been shown to be a good starting point to obtain unique insights concerning the formation of nanoparticles. However, for larger particles it becomes more challenging or impossible to count the atoms in a column in a straightforward manner. Therefore, other approaches should be explored. The use of prior knowledge in such 3D reconstruction techniques should be avoided to enable an unbiased and direct indexation of the surface facets. Recently, the atomic-scale reconstruction of a distorted icosahedral multiply twinned Au nanoparticle with a diameter of ~10 nm was reported[14]. Although not all atoms could be located in this reconstruction, valuable information concerning lattice parameters and grains inside the particle could be obtained. It must be noted however that 55 images were required to obtain this 3D reconstruction.

Here, we propose a compressive-sensing-based 3D reconstruction algorithm, which enables us to completely characterize the 3D atomic lattice of free-standing Au nanorods. On the basis of a limited number of HAADF-STEM projection images, a high-quality 3D reconstruction of the atomic structure is obtained without the use of any prior knowledge. From the final reconstruction, the surface facets of the rods can be characterized with a high precision. In addition, imperfections at the atomic scale and surface relaxation are studied. We applied our approach to Au nanorods, which have important applications in the field of nanoplasmonics, but the methodology is applicable to a wide variety of nanostructures.

As a result of their well-defined anisotropy and the interaction between shape and optical response, Au nanorods have been studied extensively[3,4,15]. We investigated Au nanorods, obtained by seed-mediated growth in aqueous solution, assisted by the surfactant cetyltrimethylammonium bromide (CTAB) and Ag^+ ions[16]. In addition, as Au nanorods prepared by seeded growth in the presence of a gemini surfactant were recently used for the analysis of nanorod crystallography[3], we also studied these for comparison. More details concerning the synthesis procedure can be found in the Methods. Electron tomography at relatively low magnification in combination with electron diffraction was used to determine the overall morphology of the rods. The details of this procedure are discussed in the Methods. The results are presented in Fig. 1a,b, revealing a faceted morphology for both types of rod, in agreement with previous reports[3,4,17]. However, the resolution that can be obtained at this magnification prevents correct indexing of the side facets of these reconstructions.

These observations are complemented by intensity profiles acquired from high-resolution HAADF-STEM images. HAADF-STEM yields a signal that is proportional to the thickness of the specimen and to the atomic mass of the atoms in the sample[18–20]. In this case, the HAADF-STEM intensity therefore corresponds to a thickness profile of the Au nanorods. For both types of nanorod, a HAADF-STEM image is acquired along a [110] zone axis as shown in Fig. 1c,e. The intensity profile acquired along the direction perpendicular to the major axis is shown in Fig. 1f,h. These results suggest that the morphology of the rod grown with CTAB is mainly composed of {110} and {100} facets as illustrated by the correspondence with the model in Fig. 1d,g, in agreement with early characterization[17]. This analysis also indicates that the morphology of the rods grown with the gemini surfactant deviates from this model structure, as recently reported[3].

[1]Electron Microscopy for Materials Research (EMAT), University of Antwerp, Groenenborgerlaan 171, 2020 Antwerp, Belgium, [2]Departamento de Química Física, Universidade de Vigo, 36310 Vigo, Spain, [3]Institute for Experimental Physics, Ulm University, Albert-Einstein-Allee 11, 89081 Ulm, Germany.
*e-mail: sara.bals@ua.ac.be.

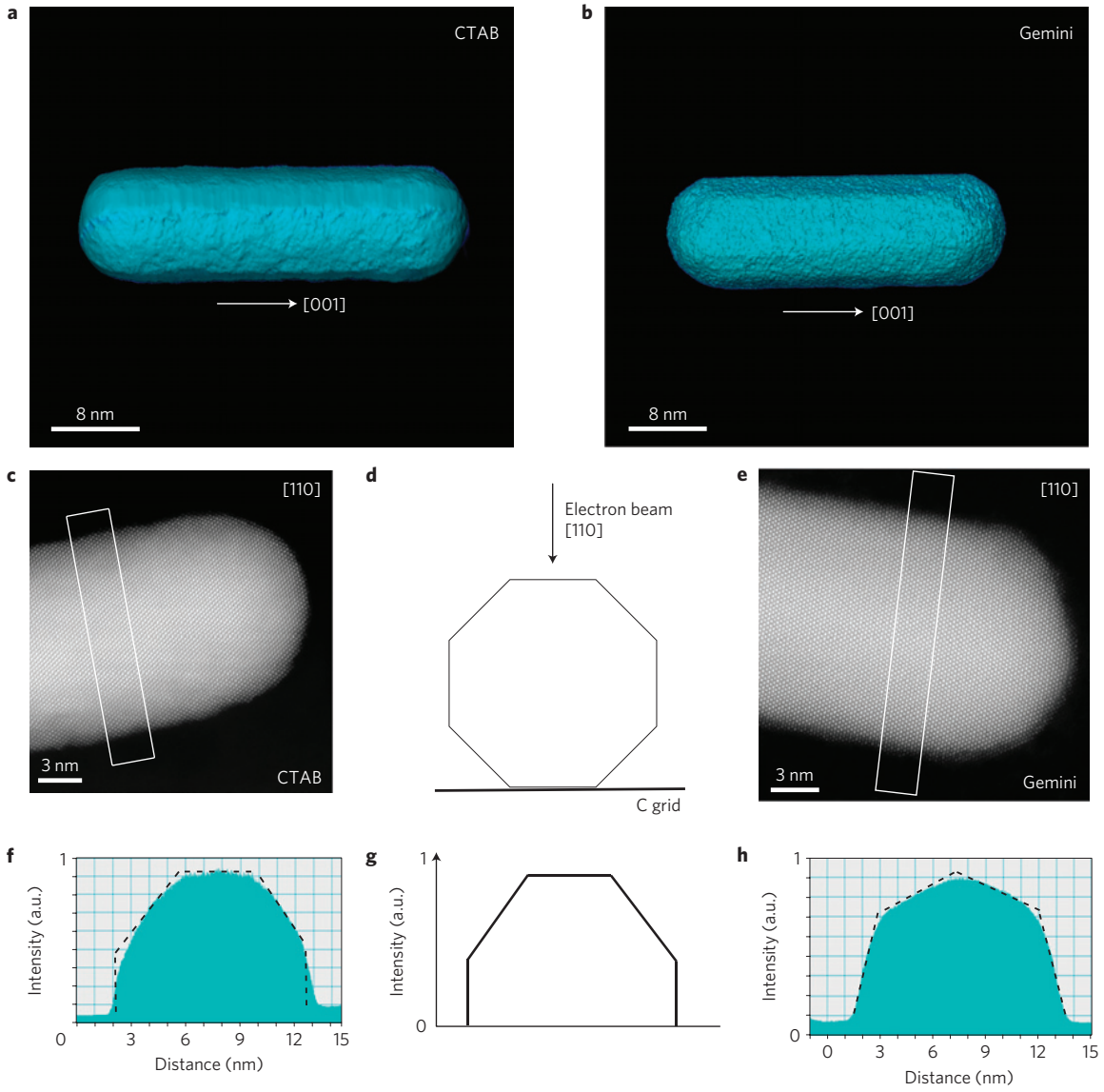

Figure 1 | Comparison between Au nanorods grown with CTAB and gemini surfactants. a,**b**, 3D visualizations of tomographic reconstructions of both types of nanorod. Crystal facets are visible in both tomographic reconstructions. **c**–**e**, High-resolution HAADF-STEM projections of both nanorods oriented along the [110] direction. **f**,**g**, The intensity profile acquired from the first projection (**f**) corresponds to a model where the morphology is composed of {110} and {100} facets (**d**,**g**). **h**, The intensity profile acquired from the projection of the rod grown with the gemini surfactant clearly shows a deviation from this model.

The analysis described above presents a first step towards the full 3D characterization of the morphology of the nanorods. Next, four different high-resolution HAADF-STEM images were acquired along different zone axes ([100], [110], [010] and [$\bar{1}$10]) for nanorods prepared using the CTAB surfactant and nanorods grown with the gemini surfactant. After alignment of the images, they are used as an input for a tomographic reconstruction algorithm based on compressive sensing[21,22]. Compressive sensing is a technique specialized in finding a solution that has a sparse representation to a set of linear equations. Recently, the advantages of using compressive sensing for electron tomography were demonstrated for reconstructions with nanoscale resolution[23,24]. For 3D reconstructions at the atomic scale, it is valid to exploit the sparsity of the object (and its 3D reconstruction) as only a limited number of voxels contain an atom and most voxels correspond to vacuum. Using this prior knowledge in a tomographic reconstruction algorithm will result in a more reliable atomic-scale reconstruction as compared with more conventional reconstruction algorithms such as the simultaneous iterative reconstruction technique[25] (SIRT). Another advantage is that because of the sparsity incorporated in the reconstruction algorithm, a very limited number of projections is sufficient to create a faithful reconstruction of the atomic lattice. It should be noted that although we assume the object to be sparse, no assumptions are made concerning the positions of the atoms.

In a conventional SIRT algorithm, one starts with a first 3D reconstruction that is re-projected along the directions of the original acquisition angles. The difference between the (2D) re-projections and the original (2D) projections is called the projection error. When using SIRT, this projection error is iteratively minimized by adding the reconstructed projection error to the previous intermediate reconstruction. Mathematically, a tomographic reconstruction corresponds to reconstructing an object x starting from its projections b, which are acquired by a projection operator A. The

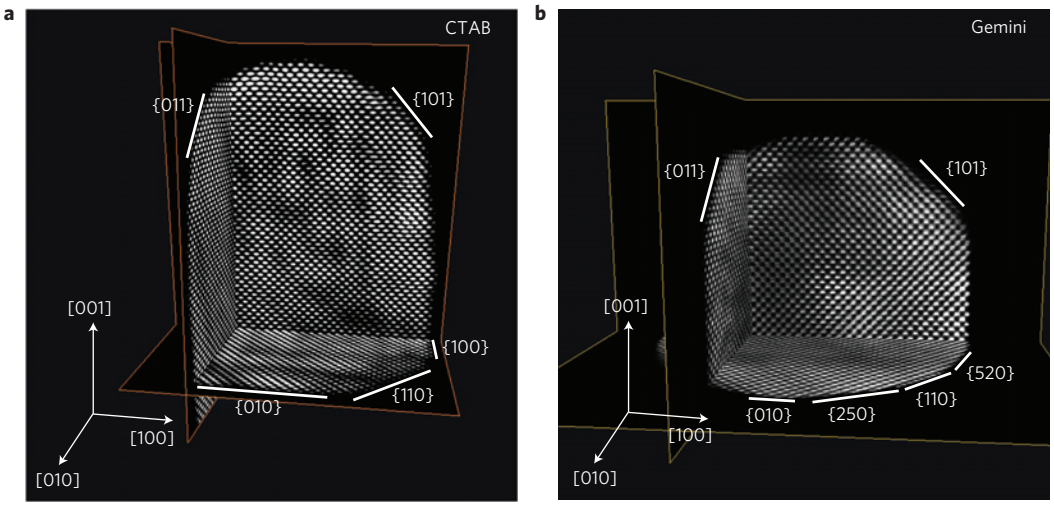

Figure 2 | 3D reconstruction of Au nanorods. a, Three orthogonal slices through the reconstruction of a nanorod grown with CTAB, showing individual atom positions. It can be seen that {110} and {100} facets compose the morphology of the rod. The tip is rounded, with clear terraces at the {101} planes. **b**, Three corresponding slices through a reconstruction of a nanorod synthesized with the gemini surfactant. For this rod a more rounded morphology of the cross-section is observed including {520} facets. The facets composing the tip of the nanorod are comparable to these of the nanorod grown with CTAB.

tomographic reconstruction then often corresponds to iteratively solving the following minimization problem.

$$\hat{x} = \underset{x}{\operatorname{argmin}} \|Ax - b\|_2^2$$

In the compressive-sensing algorithm employed in this work, an additional penalty parameter λ is introduced leading to a simultaneous minimization of the projection error and the L1-norm of the object (that is, the sum of the absolute values of all the voxels in the reconstructed object)[26]:

$$\hat{x} = \underset{x}{\operatorname{argmin}} \left[\|Ax - b\|_2^2 + \lambda \|x\|_1 \right]$$

The reliability of the reconstruction algorithm is confirmed by simulations as shown in the Supplementary Information. All atoms, and therefore also all surface facets, can be recovered in this simulation experiment.

This reconstruction algorithm was applied to the high-resolution HAADF-STEM images for both types of Au nanorod. More information on the practical implementation can be found in the Methods. A visualization of the final result is presented in Fig. 2a,b, where orthogonal slices through the 3D reconstruction of the rods synthesized with the CTAB and the gemini surfactant are presented, respectively.

From the reconstruction presented in Fig. 2a, it can be directly concluded that the cross-section of the rod grown with CTAB is bound by alternating {100} and {110} planes, as proposed previously[17]. This is in agreement with the HAADF-STEM profiles presented in Fig. 1. From the 3D reconstruction presented in Fig. 2b, the facets of the rod grown using the gemini surfactant can be characterized as {520} planes. These facets were also observed in a previous study[3] where high-resolution transmission electron microscopy was performed on Au nanorods standing perpendicular on the support grid. As can be observed in Fig. 2, the tip of both nanorods has a rounded morphology with well-defined terraces corresponding to {110} facets.

For the reconstruction obtained for the nanorod grown using CTAB, a 3D Fourier transform was calculated. Projections from this Fourier transform are shown in Fig. 3a–c. An animated view of the 3D Fourier transform can be found in the Supplementary Information. The projections of the Fourier space along the [100], [110] and [111] directions are in good agreement with the theoretical models for a face-centred-cubic (fcc) crystal lattice, which are illustrated in Fig. 3d–i. A 3D model of the reciprocal lattice is illustrated in Fig. 3d–f whereas projections of the reciprocal lattice are presented in Fig. 3g–i. The correspondence between the model and the experimental Fourier transform of the tomographic reconstruction is remarkable because no prior knowledge about the crystal structure was used during the reconstruction process. The ability to characterize the boundary facets at the atomic scale is of great importance to understand the growth, reactivity and adsorption properties of these nanorods. In fact, observation of different types of boundary facet for nanorods obtained through slightly different synthetic procedures raises further questions regarding nanocrystal growth and stability.

Although the facets composing the morphology can be clearly recognized in the final reconstructions, also more detailed information at the atomic scale can be extracted from the reconstruction. Figure 4c, corresponding to a more detailed view of Fig. 4a,b, reveals the presence of an atomic surface step with a thickness of two atomic layers. This surface terrace is located at a {001} side facet and it is clear that this step will have an impact on the surface energy and many related nanoscale phenomena, including catalytic, mechanical and electronic properties[27,28].

It is important to note that the atom positions are not assumed to be fixed during the reconstruction process. Therefore, the reconstruction presented in Fig. 2 can serve as a starting point to investigate strain in three dimensions. Here, we apply the geometrical phase analysis (GPA) to a 3D reconstruction rather than to a 2D projection of a 3D object[29,30]. More details on the approach and its reliability can be found in the methodology section, whereas the reliability of the approach is discussed, on the basis of simulation experiments, in the Supplementary Information. By selecting three reflections for GPA analysis, we obtain the full 3D ε_{zz} strain field, which is presented in Fig. 4d. A reference region where no strain is present was selected in the middle of the nanorod. This implies that all strain measurements are relative with respect to this reference region. The colour code in Fig. 4d corresponds to the strain in the nanorod and is scaled between −3% (blue) and +3% (red). The error on these measurements is estimated through simulation experiments (as explained in the Supplementary Information) and equals ±1.3%. It is likely that

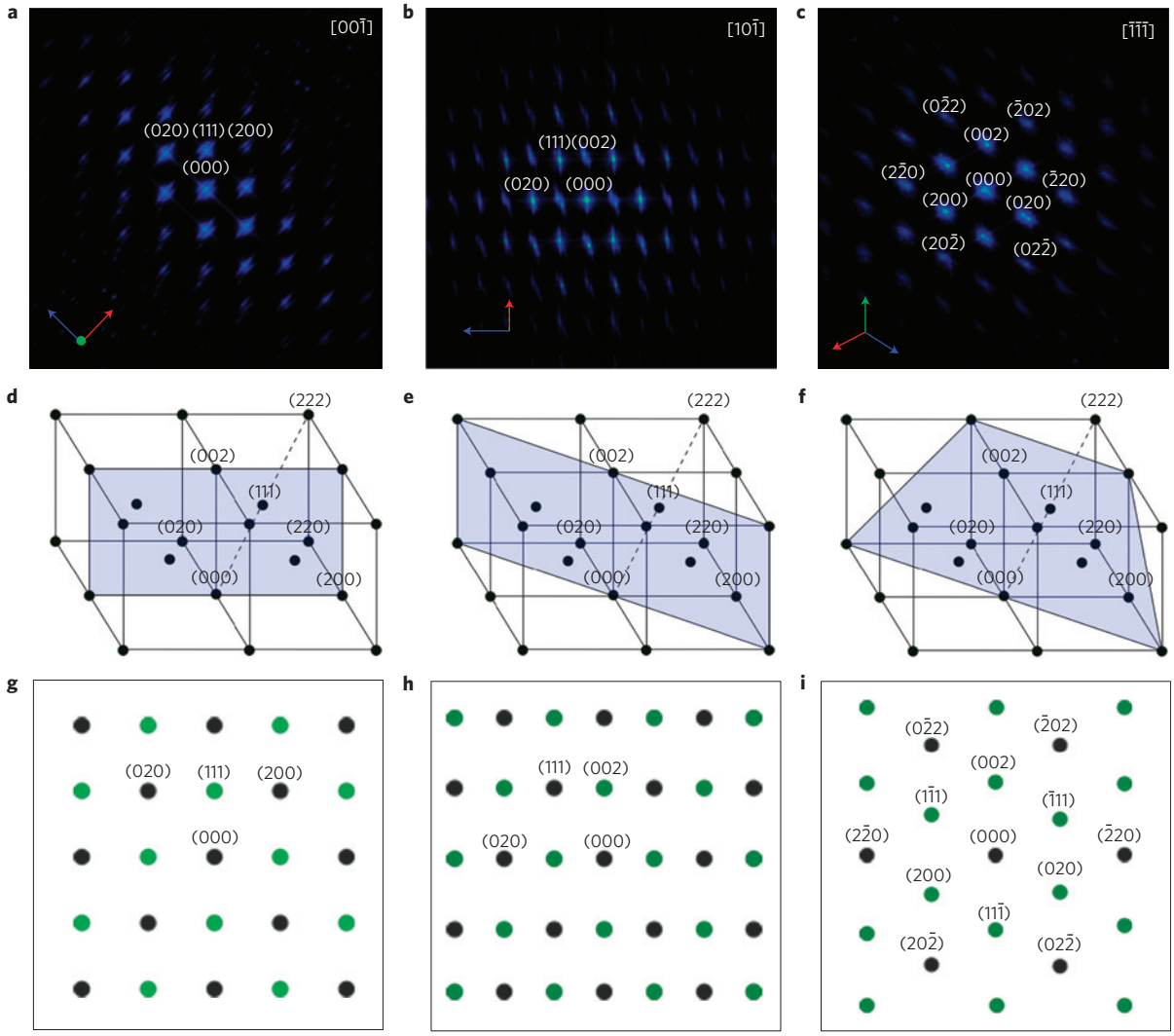

Figure 3 | 3D Fourier transform of the reconstructed CTAB nanorod. a–c, Projections of the calculated 3D Fourier transforms of the reconstructed nanorod obtained along different directions. **d–f**, Theoretical model corresponding to the 3D reciprocal space of an fcc crystal structure. The plane indicated in blue represents the central plane through the reciprocal space perpendicular to the projection directions of **a–c**. **g–i**, Schematic illustrations of the projections of the Fourier transform along the projection directions of **a–c**. The grey reflections are present in the blue layer as indicated in **d–f** whereas the green reflections are located above or below this central layer.

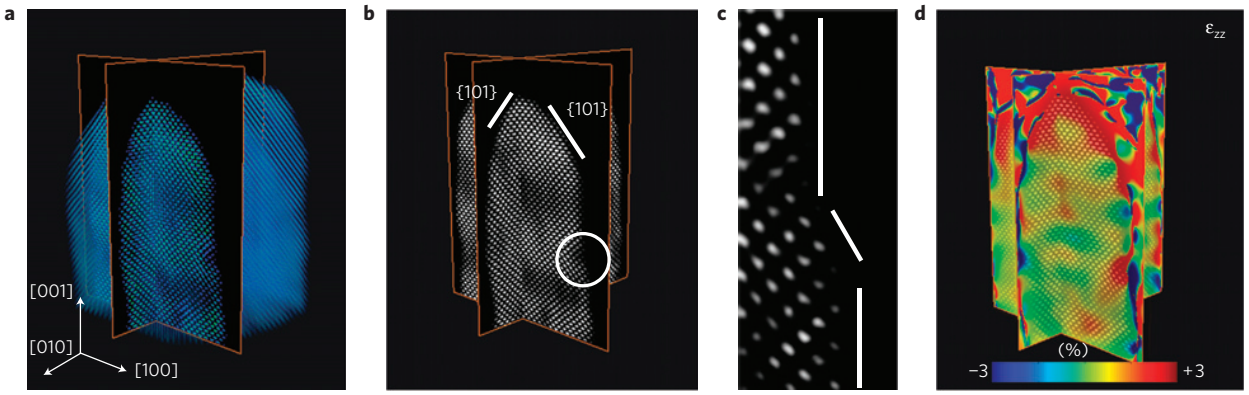

Figure 4 | Atomic-resolution reconstruction of a Au nanorod. a, Volume rendering of the reconstructed nanorod with two selected slices through the reconstruction. **b**, The two slices from **a** show that the tip of the nanorod is composed of {101} facets. A region with an atomic surface step is indicated. **c**, A more detailed view of the region encircled in **b**. In this region, a surface step with a thickness of two atoms is observed in the tomographic reconstruction. **d**, Slices through the 3D ε_{zz} strain measurement indicating an outward relaxation of the atoms at the tip of the nanorod.

because of this uncertainty the strain field in the centre of the nanorod shows slight deviations from the equilibrium value. The corresponding reconstructed atomic lattice is shown in Fig. 4a,b. Figure 4a shows a 3D rendering, whereas in Fig. 4b orthoslices through the reconstruction are presented. This atomic-scale 3D reconstruction in combination with the 3D ε_{zz} strain field provides unique information about the relationship between the atomic lattice and the intrinsic strain present in the nanorod. For example, it is clear that the tip of the nanorod is (approximately 3%) positively strained at its end. The measured anisotropy present in the ε_{zz} strain map may be of importance towards understanding the optical properties of the nanorods[1,31].

Using high-resolution HAADF-STEM projection images the fcc crystal lattice of the Au nanorods has been reproduced without prior knowledge of the atomic structure. In this way the side facets of the rods have been precisely determined. Using our approach, 3D strain measurements can be obtained and correlated to the atomic lattice of a nano-object. Although the methodology proposed is applied only to pure Au nanorods, it clearly opens perspectives for the 3D atomic visualization of different nanomaterials, including intermetallics, core–shell nanoparticles and bimetallic nanocrystals. Further options are the 3D measurement of surface relaxation at nanomaterials, hopefully leading to a better understanding of the opto-electronic properties of some of these materials.

Methods

Sample preparation. Au nanorods were synthesized using the well-known seeded-growth method[16]. Au nanorods with {520} boundary facets were prepared by overgrowth in the presence of a gemini surfactant, as recently reported[32]. The nanorods were then dispersed in H_2O, deposited on a C grid and plasma cleaned with a H_2/O_2 gas mixture for 15 s.

Low-magnification tomography. A low-magnification HAADF-STEM tilt series was acquired in the HAADF-STEM mode as described previously. The tilt angles for the CTAB-synthesized rod ranged from −75° to +60° with a 5° tilt increment. For the nanorod grown with gemini, the tilt series ranges between −72° and +74° with an increment of 2° between two successive tilt angles. Alignment of the tilt series was done using a combination of cross-correlation methods in FEI Inspect3D and a manual alignment performed in the IMOD software[33]. The reconstruction was performed with a total variation minimization reconstruction algorithm to minimize artefacts in the reconstruction[23]. Before image acquisition, an electron diffraction pattern was recorded to facilitate indexing of the final reconstructions.

HAADF-STEM imaging. HAADF-STEM imaging was performed at an aberration-corrected cubed FEI Titan 50-80 operated at 300 kV. During the tilt experiments, the investigated samples were mounted on a motorized rotation tomography Fischione 2040 holder. This holder can both rotate the sample in plane and tilt the sample over an angular range of ±75° enabling us to reach four different major zone axes. The four zone axes that are used correspond to the [100], the [110], the [010] and the [$\bar{1}$10] axis. A probe semi convergence angle of 21.4 mrad was used during the acquisition. The HAADF detector was mounted at a camera length of 110 mm to guarantee incoherent imaging of the Au nanorod. To reduce sample drift during the experiment, the specimen holder was allowed to relax after each tilting step for several minutes before image acquisition.

High-resolution tomography. The 3D atomic lattice of the Au nanorods is determined using a compressive-sensing-based reconstruction algorithm where four HAADF-STEM projections are used as input. Alignment of the images was done by calculating the centre of mass in each projection as proposed previously[14]. The reconstructions were calculated on the basis of the iterative compressive-sensing algorithm as explained above. This algorithm was implemented in Matlab using a penalty parameter λ of 0.5. Earlier work and simulation experiments showed that this is a suitable value[23]. To minimize remaining fanning artefacts for the reconstruction shown in Fig. 2b, a convolution in Fourier Space was carried out with the reconstruction shown in Fig. 1b. More details on the implementation and simulation experiments confirming the validity of this reconstruction technique are provided in the Supplementary Information.

GPA. 3D GPA was implemented in Matlab by selecting three reciprocal lattice points. During the 3D GPA analysis, a Gaussian selection window was used with such a diameter that the spatial resolution of the strain determination equals 1 nm.

Received 29 June 2012; accepted 17 September 2012; published online 21 October 2012

References

1. Pecharroman, C., Perez-Juste, J., Mata-Osoro, G., Liz-Marzan, L. M. & Mulvaney, P. Redshift of surface plasmon modes of small gold rods due to their atomic roughness and end-cap geometry. *Phys. Rev. B* **77,** 035418 (2008).
2. Chang, L. Y., Barnard, A. S., Gontard, L. C. & Dunin-Borkowski, R. E. Resolving the structure of active sites on platinum catalytic nanoparticles. *Nano. Lett.* **10,** 3073–3076 (2010).
3. Carbo-Argibay, E. *et al.* The crystalline structure of gold nanorods revisited: Evidence for higher-index lateral facets. *Angew. Chem. Int. Ed.* **49,** 9397–9400 (2010).
4. Katz-Boon, H. *et al.* Three-dimensional morphology and crystallography of gold nanorods. *Nano Lett.* **11,** 273–278 (2011).
5. Batson, P. E., Dellby, N. & Krivanek, O. L. Sub-ångstrom resolution using aberration corrected electron optics. *Nature* **418,** 617–620 (2002).
6. Erni, R., Rossell, M. D., Kisielowski, C. & Dahmen, U. Atomic-resolution imaging with a Sub-50-pm electron probe. *Phys. Rev. Lett.* **102,** 096101 (2009).
7. Valden, M., Lai, X. & Goodman, D. W. Onset of catalytic activity of gold clusters on titania with the appearance of nonmetallic properties. *Science* **281,** 1647–1650 (1998).
8. Grzelczak, M., Perez-Juste, J., Mulvaney, P. & Liz-Marzan, L. M. Shape control in gold nanoparticle synthesis. *Chem. Soc. Rev.* **37,** 1783–1791 (2008).
9. Midgley, P. A. & Dunin-Borkowski, R. E. Electron tomography and holography in materials science. *Nature Mater.* **8,** 271–280 (2009).
10. Midgley, P. A. & Weyland, M. 3D electron microscopy in the physical sciences: The development of Z-contrast and EFTEM tomography. *Ultramicroscopy* **96,** 413–431 (2003).
11. Midgley, P. A., Ward, E. P. W., Hungria, A. B. & Thomas, J. M. Nanotomography in the chemical, biological and materials sciences. *Chem. Soc. Rev.* **36,** 1477–1494 (2007).
12. Van Aert, S., Batenburg, K. J., Rossell, M. D., Erni, R. & Van Tendeloo, G. Three-dimensional atomic imaging of crystalline nanoparticles. *Nature* **470,** 374–377 (2011).
13. Bals, S. *et al.* Three-dimensional atomic imaging of colloidal core-shell nanocrystals. *Nano. Lett.* **11,** 3420–3424 (2011).
14. Scott, M. C. *et al.* Electron tomography at 2.4-ångström resolution. *Nature* **483,** 444–447 (2012).
15. Perez-Juste, J., Pastoriza-Santos, I., Liz-Marzan, L. M. & Mulvaney, P. Gold nanorods: Synthesis, characterization and applications. *Coordin. Chem. Rev.* **249,** 1870–1901 (2005).
16. Nikoobakht, B. & El-Sayed, M. A. Preparation and growth mechanism of gold nanorods (NRs) using seed-mediated growth method. *Chem. Mater.* **15,** 1957–1962 (2003).
17. Wang, Z. L., Mohamed, M. B., Link, S. & El-Sayed, M. A. Crystallographic facets and shapes of gold nanorods of different aspect ratios. *Surf. Sci.* **440,** L809–L814 (1999).
18. Hartel, P., Rose, H. & Dinges, C. Conditions and reasons for incoherent imaging in STEM. *Ultramicroscopy* **63,** 93–114 (1996).
19. Krivanek, O. L. *et al.* Atom-by-atom structural and chemical analysis by annular dark-field electron microscopy. *Nature* **464,** 571–574 (2010).
20. Nellist, P. D. & Pennycook, S. J. The principles and interpretation of annular dark-field Z-contrast imaging. *Adv. Imag. Elect. Phys.* **113,** 147–203 (2000).
21. Candes, E. J. & Wakin, M. B. An introduction to compressive sampling. *IEEE Signal Proc. Mag.* **25,** 21–30 (2008).
22. Donoho, D. L. Compressed sensing. *IEEE Trasns. Inform. Theory* **52,** 1289–1306 (2006).
23. Goris, B., Van den Broek, W., Batenburg, K. J., Mezerji, H. H. & Bals, S. Electron tomography based on a total variation minimization reconstruction technique. *Ultramicroscopy* **113,** 120–130 (2012).
24. Saghi, Z. *et al.* Three-Dimensional morphology of iron oxide nanoparticles with reactive concave surfaces. A compressed sensing-electron tomography (CS-ET) approach. *Nano Lett.* **11,** 4666–4673 (2011).
25. Gilbert, P. Iterative methods for the three-dimensional reconstruction of an object from projections. *J. Theoret. Biol.* **36,** 105–117 (1972).
26. Kim, S. J., Koh, K., Lustig, M., Boyd, S. & Gorinevsky, D. An interior-point method for large-scale l(1)-regularized least squares. *IEEE J-Stsp* **1,** 606–617 (2007).
27. Seo, J. *et al.* Transmission of topological surface states through surface barriers. *Nature* **466,** 343–346 (2010).
28. Alivisatos, A. P. Semiconductor clusters, nanocrystals, and quantum dots. *Science* **271,** 933–937 (1996).
29. Hytch, M. J., Snoeck, E. & Kilaas, R. Quantitative measurement of displacement and strain fields from HREM micrographs. *Ultramicroscopy* **74,** 131–146 (1998).
30. Johnson, C. L. *et al.* Effects of elastic anisotropy on strain distributions in decahedral gold nanoparticles. *Nature Mater.* **7,** 120–124 (2008).

31. Ouyang, G., Zhu, W. G., Sun, C. Q., Zhu, Z. M. & Liao, S. Z. Atomistic origin of lattice strain on stiffness of nanoparticles. *Phys. Chem. Chem. Phys.* **12,** 1543–1549 (2010).
32. Guerrero-Martinez, A., Perez-Juste, J., Carbo-Argibay, E., Tardajos, G. & Liz-Marzan, L. M. Gemini-surfactant-directed self-assembly of monodisperse gold nanorods into standing superlattices. *Angew. Chem. Int. Ed.* **48,** 9484–9488 (2009).
33. Kremer, J. R., Mastronarde, D. N. & McIntosh, J. R. Computer visualization of three-dimensional image data using IMOD. *J. Struct. Biol.* **116,** 71–76 (1996).

Acknowledgements

We thank A. Rosenauer from IFP, Bremen, for the use of the STEMsim program and A. Béché from FEI for his technical advice. The work was supported by the Flemish Fund for Scientific Research (FWO Vlaanderen) through a PhD research grant to B.G. G. Van Tendeloo acknowledges financial support from the European Research Council (ERC Advanced Grant 24691—COUNTATOMS). L.M.L-M. acknowledges financial support from the European Research Council (ERC Advanced Grant 267867—PLASMAQUO). The authors appreciate financial support from the European Union under the Seventh Framework Program (Integrated Infrastructure Initiative N. 262348 European Soft Matter Infrastructure, ESMI). The authors also acknowledge financial support from the Flemish Hercules 3 programme for large infrastructure.

Author contributions

B.G. and S.B. performed the experiments and analysed the 3D reconstructions, B.G. and W.V.d.B. developed the reconstruction algorithm, E.C-A., S.G-G. and L.M.L-M. carried out particle synthesis and interpreted the results, G.V.T. contributed to the methodology, the interpretation and to the redaction. All the authors read and commented on the paper.

Additional information

Supplementary information is available in the online version of the paper. Reprints and permissions information is available online at www.nature.com/reprints. Correspondence and requests for materials should be addressed to S.B.

Competing financial interests

The authors declare no competing financial interests.